The Astrophysical Journal, 743:108 (15pp), 2011 December 20 doi:10.1088/0004-637X/743/2/108

INTERACTIONS BETWEEN FORMING STARS AND DENSE GAS IN THE SMALL LOW-MASS CLUSTER CEDERBLAD 110

E. F. Ladd[1], T. Wong[2], T. L. Bourke[3], and K. L. Thompson[4]
[1] Department of Physics and Astronomy, Bucknell University, Lewisburg, PA 17837, USA; ladd@bucknell.edu
[2] Department of Astronomy, University of Illinois, Urbana, IL 61801, USA
[3] Harvard-Smithsonian Center for Astrophysics, 60 Garden Street, Cambridge, MA 02138, USA
[4] Department of Physics and Astronomy, University of Kentucky, Lexington, KY 40506, USA
Received 2011 June 13; accepted 2011 September 8; published 2011 November 29

ABSTRACT

We present observations of dense gas and outflow activity in the Cederblad 110 region of the Chamaeleon I dark cloud complex. The region contains nine forming low-mass stars in evolutionary stages ranging from Class 0 to Class II/III crowded into a 0.2 pc region with high surface density ($\Sigma_{\rm YSO} \sim 150$ pc^{-2}). The analysis of our N_2H^+ ($J = 1 \rightarrow 0$) maps indicates the presence of 13 ± 3 solar masses of dense ($n \sim 10^5$ cm^{-3}) gas in this region, much of which is unstable against gravitational collapse. The most unstable material is located near the Class 0 source MMS-1, which is almost certainly actively accreting material from its dense core. Smaller column densities of more stable dense gas are found toward the region's Class I sources, IRS 4, 11, and 6. Little or no dense gas is colocated with the Class II and III sources in the region. The outflow from IRS 4 is interacting with the dense core associated with MMS-1. The molecular component of the outflow, measured in the ($J = 1 \rightarrow 0$) line of ^{12}CO, appears to be deflected by the densest part of the core, after which it appears to plow through some of the lower column density portions of the core. The working surface between the head of the outflow lobe and the dense core material can be seen in the enhanced velocity dispersion of the dense gas. IRS 2, the Class III source that produces the optical reflection nebula that gives the Cederblad 110 region its name, may also be influencing the dense gas in the region. A dust temperature gradient across the MMS-1 dense core is consistent with warming from IRS 2, and a sharp gradient in dense gas column density may be caused by winds from this source. Taken together, our data indicate that this region has been producing several young stars in the recent past, and that sources which began forming first are interacting with the remaining dense gas in the region, thereby influencing current and future star formation activity.

Key words: ISM: individual objects: Ced 110 – ISM: individual objects: Chamaeleon I – ISM: jets and outflows – ISM: kinematics and dynamics

Online-only material: color figures

1. INTRODUCTION

Stars form from the densest environments in molecular clouds, often clustered together spatially in groups ranging from a few sources to many thousands, and together temporally over a relatively short period of time. It is now well established that most stars form in embedded clusters (e.g., Lada & Lada 2003), where the term "cluster" is commonly defined with a threshold value in young stellar object (YSO) density ranging from 3 to 30 YSOs pc^{-2} (Carpenter 2000; Lada & Lada 2003; Jorgensen et al. 2008). In some regions, the density is high enough that it is likely forming stars will pass within a star-forming core radius ($\sim$0.05 pc) of a neighbor during their $\sim$100,000 year formation lifetimes (Gutermuth et al. 2005). The possibility of close encounters in rich regions has led several authors to consider how these encounters might affect the formation process, perhaps through the truncation of circumstellar disks, or disruption of binary systems (e.g., Allen et al. 2007). Star formation in the cluster environment may provide energetic feedback on cluster gas and dust; the enhanced dense gas velocity dispersions in cluster material, and the anticorrelation between YSO surface density and dense gas column density for more evolved sources are indications of this feedback (Gutermuth et al. 2005). The dynamics in the largest clusters are also complicated by the presence of massive stars, whose stellar winds and ionizing radiation can impact a large fraction of a cluster's volume (Wang et al. 2008).

Clustering occurs on smaller scales as well, and while smaller clusters typically do not harbor massive stars, they can have large YSO surface densities (e.g., Chen & Tokunaga 1994; Gutermuth et al. 2009; Kirk & Myers 2011). With multiple stars forming in close proximity, interactions between even these lower mass stars may influence their evolution. Recently, Bressert et al. (2010) have shown that the histogram of YSO surface density in nearby star-forming clouds is centrally peaked and consistent with a lognormal distribution peaking at $\Sigma_{\rm YSO} = 22$ pc^{-2}; that is, there appears to be no evidence for functionally distinct "isolated" and "clustered" modes of star formation, but instead star formation takes place over a smoothly distributed continuum of YSO surface densities. Thus, it is reasonable to ask whether the interactions that characterize star formation in large clusters at high surface density might also operate, albeit reduced in intensity and effect, in less rich environments.

We present a study of the forming stars and dense gas in the Cederblad 110 region in the Chamaeleon I molecular cloud, a small grouping of $\sim$10 forming stars, each of relatively low mass, but tightly grouped together with high surface density. Our goal is to assess how the currently forming stars may be affecting one another and how they might influence subsequent star formation in the region.

1.1. The Ced 110 Region

The Ced 110 star-forming region of the Chamaeleon I molecular cloud is located just east of the optical reflection nebula that

provides its name (Cederblad 1946). The Chamaeleon I cloud, with a mass of ∼1000 $M_\odot$ (Mizuno et al. 2001; Belloche et al. 2011) is one of the most nearby regions of star formation, at a distance of 160 pc (Whittet et al. 1997; Knude & Hog 1998). Dust extinction, $C^{18}O$ emission, and submillimeter dust continuum mapping of this cloud show that the Ced 110 region has the highest column density and the most concentrated gas and dust mass in the cloud (Kainulainen et al. 2006; Haikala et al. 2005; Belloche et al. 2011).

The Ced 110 region is actively forming stars in close proximity, with nine YSOs at a variety of evolutionary stages clustered within 0.2 pc (see Figure 1). This collection of objects forms a rather tightly packed subset of the "ChaI Group 2," a collection of 96 YSOs identified by Kirk & Myers (2011) that spans much of the southern portion of the Chamaeleon I cloud. The YSO surface density $\Sigma_{YSO} = 157$ pc^{-2}, a value considerably larger than the mean YSO surface density of 22 pc^{-2} for all forming stars within 500 pc (Casertano & Hut 1985; Bressert et al. 2010). In the northwestern part of the grouping, IRS 2 (J11061540-7721567) is a Class III object of spectral type G3-G7 (Luhman 2008) producing the Ced 110 optical reflection nebula. In addition to being the most evolved of the sources in the region, IRS 2 is also the most luminous and probably the most massive. Along the eastern and southern periphery are Class II sources J11062942-7724586, J11070369-7724307, and the flat spectrum, nearly Class II sources ISO 97[5] and ISO 101 (Persi et al. 2000; Luhman et al. 2008; Hiramatsu et al. 2007). The three Class I sources IRS 6,[6] IRS 11, and IRS 4 form a nearly east–west line in the center of the region. Of these three, IRS 6 is likely the most evolved, with an infrared spectral slope that is flatter than those of IRS 11 and IRS 4 (Luhman et al. 2008), and a higher bolometric temperature ($T_{bol} = 260$ K; Lehtinen et al. 2001). Near-infrared images of IRS 4 show bipolar reflection nebulosity suggesting it is a disk system with a nearly edge-on orientation (Zinnecker et al. 1999; Persi et al. 2001). A bipolar molecular outflow has been attributed to this source by many authors (Mattila et al. 1989; Prusti et al. 1991; Belloche et al. 2006; Hiramatsu et al. 2007). The Class 0 source MMS-1, first detected in the millimeter continuum by Reipurth et al. (1996), and since at 24 and 70 μm (Belloche et al. 2006), is clearly the youngest source in the region.

This subgrouping of objects lies in a region of high visual extinction (Kainulainen et al. 2006; Belloche et al. 2011) and strong and extended far-infrared and millimeter continuum emission (Kontinen et al. 2000; Belloche et al. 2011). From their 870 μm continuum measurements, Belloche et al. (2011) identify an elongated high column density structure with size 0.6×0.2 pc, position angle 60°, and mass 19 $M_\odot$. This structure has also been identified by Mizuno et al. (1999) and Haikala et al. (2005) in cloudwide surveys of $C^{18}O$ ($J = 1 \rightarrow 0$) emission. Haikala et al. (2005) estimate a mass of 12 $M_\odot$ and a radius of 0.2 pc for the $C^{18}O$ core. Smaller maps covering only the southern portion of the subgrouping have been carried out in HC_3N (Kontinen et al. 2000), HCN, and HNC (Tennekes et al. 2006). Detections in these lines show that dense gas ($n \gtrsim 10^5$ cm^{-3}) is present in this region. Tennekes et al. (2006) also present NH_3 (J, K) = (1,1) and (2,2) spectra from which they derive a kinetic temperature $T_K = 12$ K for the dense gas.

[5] This source was detected as a binary with 2″ separation in the mid-infrared by Haisch et al. (2006). They report that the secondary has steeper spectral index than the primary. For this paper, which deals with structures on much larger spatial scales, we will consider this as a single system.

[6] This source was detected as a binary with 2″ separation in the mid-infrared by Haisch et al. (2006). They report that both components have steep spectral slopes suggesting Class I status. For this paper, which deals with structures on much larger spatial scales, we will consider this as a single system.

2. OBSERVATIONS

We observed the Ced 110 region in the ($J = 1 \rightarrow 0$) lines of ^{12}CO, $C^{18}O$, and N_2H^+. The observations were conducted during the 2004 and 2005 observing seasons with the 22 m ATNF Mopra Telescope equipped with a dual polarization superconductor–insulator–superconductor receiver operating in the 85–115 GHz frequency range. We constructed 5′ × 5′ maps using the newly implemented on-the-fly observing technique, with spectra taken at 2 s intervals as the telescope scanned across the sky. Spectra were spaced by 6″ so that the Mopra main beam (36″ at 92 GHz and 33″ at 115 GHz) was well oversampled in the scanning direction; the row spacing was 10″, also oversampling the beam. Each row was preceded by an off-source integration at a location about 0.5°–1° from the map center, chosen to be free of CO emission based on large-scale CO maps (Mizuno et al. 2001). Typical single-sideband system temperatures, measured by comparing blank sky with an ambient load, were $T_{sys} = 200$ K for N_2H^+ and 600 K for the CO isotopomers. Prior to each map, which took a total of 75 minutes to complete, the antenna pointing was checked on the SiO maser R Car; typical corrections were less than 5″. We made eight maps in ^{12}CO and $C^{18}O$, and five in N_2H^+. Half of the maps were scanned in the right ascension direction, while the other half were scanned in the declination direction, in order to reduce any striping effects in the combined data sets.

The digital correlator was configured to output 1024 channels across 64 MHz for most of the ^{12}CO observations and across 16 MHz for the N_2H^+ and $C^{18}O$ observations. However, some of the ^{12}CO observations were made in 16 MHz mode and then rebinned to 64 MHz before combining with the other maps. All three data sets were then Hanning smoothed in the frequency domain for final spectral sampling of 130 kHz (0.32 km s^{-1}) for the ^{12}CO data set, 31 kHz (0.08 km s^{-1}) for the $C^{18}O$ data set, and 31 kHz (0.10 km s^{-1}) for the N_2H^+ data set.

Before processing the individual spectra into a datacube, the position information (generally recorded at times slightly offset from the time of each spectral integration) was linearly interpolated to the time of the midpoint of each integration using FORTRAN programs based on the ATNF RPFITS libraries. Subsequent spectral processing (baselining and calibration onto a T_A^* scale) was performed using the *LiveData* task in AIPS++, and the spectra were gridded into datacubes with 12″ spacing using the AIPS++ *Gridzilla* task. For the $C^{18}O$ and ^{12}CO observations, we used an 18″ full width at half-maximum (FWHM) Gaussian smoothing kernel truncated at a radius of 18″ to produce the gridded datacube. The effective resolution of the resulting maps, determined by simulating an observation of a point source and processing it through the *LiveData* and *Gridzilla* pipeline, is 40″ for the $C^{18}O$ data and 37″ for the ^{12}CO data. The N_2H^+ data were gridded with a larger 36″ Gaussian kernel truncated at a radius of 36″, and the effective resolution of this data set is 49″.

The data were rescaled onto a T_{MB} scale using the "extended beam" efficiency of $\eta_{xb} = 0.55$ for the spatially extended $C^{18}O$ emission, a "main-beam" efficiency of $\eta_{mb} = 0.42$ for the ^{12}CO (since we are mainly interested in the spatially localized outflow emission in these data), and $\eta_{mb} = 0.46$ for the lower frequency N_2H^+ data (Ladd et al. 2005). For all three data sets, a linear baseline was removed from each spectrum, and an estimate of the rms noise level was obtained from the variance in intensity in

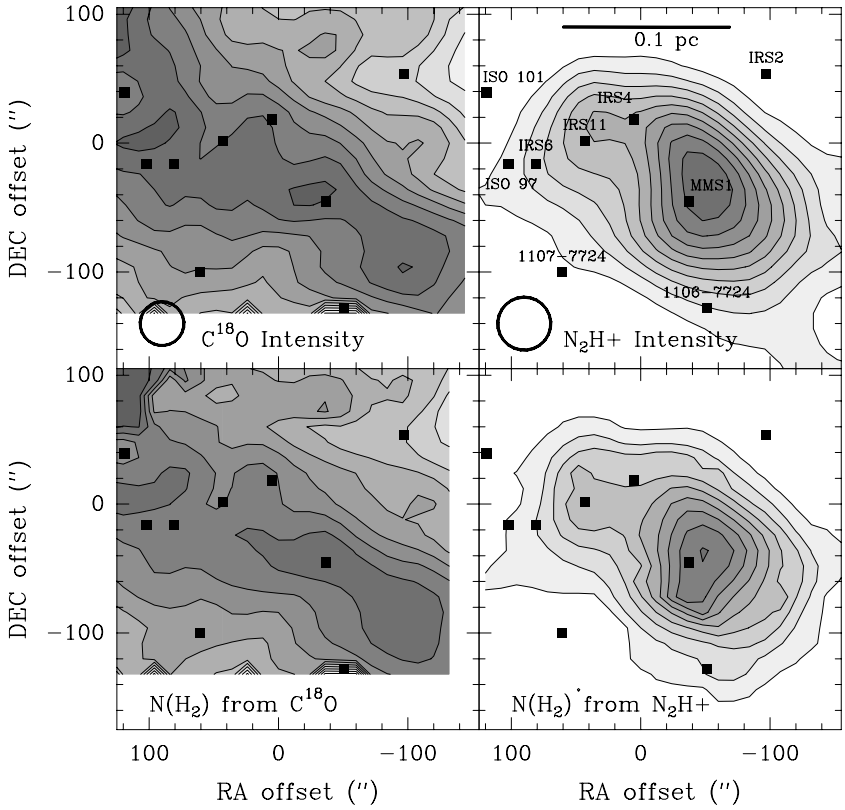

Figure 1. Maps of the integrated intensity and total column density in the Ced 110 region. Top left: $C^{18}O$ ($J = 1 \rightarrow 0$) integrated intensity. Top right: N_2H^+ ($J = 1 \rightarrow 0$) integrated intensity. Bottom left: total H_2 column density inferred from the $C^{18}O$ emission. Bottom right: total H_2 column density inferred from the N_2H^+ emission. The $C^{18}O$ intensity is integrated over the velocity range $3.5 < V_{LSR} < 5.5$ km s^{-1} and has a peak value of 2.1 K km s^{-1}. The N_2H^+ emission is integrated over all seven hyperfine components and has a peak value of 10.8 K km s^{-1}. The maximum column density in the bottom left panel is 1.5×10^{22} cm^{-2} and is found at the position of MMS-1. The peak column density in the bottom right panel is 8.5×10^{22} cm^{-2}. Contours in each panel start at 10% of peak value and increment by 10%, except for the lower left panel, where contours start at 20% of peak value and increment by 10%. Filled squares mark the positions of the YSOs in this region.

line-free portions of each spectrum. The resulting rms sensitivity (T_{MB}) of the observations is 0.31 K per 0.32 km s^{-1} channel for ^{12}CO, 0.4 K per 0.08 km s^{-1} channel for $C^{18}O$, and 0.12 K per 0.1 km s^{-1} channel for N_2H^+.

3. RESULTS

Integrated intensity maps drawn from the $C^{18}O$ and N_2H^+ datacubes are shown in the top panels of Figure 1. The $C^{18}O$ emission integrated over the line core is shown in the left panel. The emission is spatially extended and defines a broad ridge extending along a northeast–southwest axis. Larger scale maps show that this ridge extends for nearly 20′ (∼1 pc) and comprises the largest and most massive dense structure in the Chamaeleon I cloud (Haikala et al. 2005). The intensity decreases to the northwest and southeast, but drops to only ∼50% of peak intensity at the edges of the mapped region. The integrated intensity from all of the hyperfine components of the N_2H^+ emission is shown in the top right panel. This emission is much more localized, with a peak very near to the position of the millimeter and far-infrared source MMS-1. The N_2H^+ emission is also extended along a northeast–southwest axis, though the strongest emission is not centered within the $C^{18}O$ ridge, but rather displaced to the northwest toward the optically visible source IRS 2.

3.1. $C^{18}O$ Observations

All spectral line data sets were analyzed with the CLASS and GREG components of the GILDAS spectral line analysis package (http://www.iram.fr/IRAMFR/GILDAS/). A single Gaussian model was fitted to each $C^{18}O$ spectrum with the total integrated intensity, line center velocity, and FWHM line width as free parameters. In the region containing the youngest stars (MMS-1, IRS 4, and IRS 11), the spectra are well fit by a single Gaussian model and the measured line center velocity is remarkably constant with a value of $V_{LSR} = 4.36 \pm 0.04$ km s^{-1}. Along the ridge to the northeast and southwest, the fitted line center velocities are substantially higher, with typical values of $V_{LSR} = 4.50$ km s^{-1}. The measured FWHM line widths are also rather consistent over the region containing the young stars, with values of $\Delta V = 0.6 \pm 0.1$ km s^{-1}. In contrast, the spectra in the northern part of the map are broader, less symmetric, and not well fit by a single Gaussian model.

The fit parameters were used to determine the total column density of $C^{18}O$, and using an assumed abundance ratio, total H_2 column density, $N(H_2)$. Assuming that $C^{18}O$ is in local thermodynamic equilibrium (LTE) with an excitation temperature of 12 K (based on the Tennekes et al. 2006 NH_3 measurement), we calculate a peak $C^{18}O$ column density $N(C^{18}O) = 1.1 \times 10^{15}$ cm^{-2}. From a comparison between near-infrared extinction and $C^{18}O$ column density over the whole Chamaeleon I cloud, Kainulainen et al. (2006) determine the following relationship:

$$N(H_2) = 4.9 \times 10^6 N(C^{18}O) + 2.3 \times 10^{21}.$$

This relationship is similar to that found by Frerking et al. (1982) for the Taurus cloud, though the inferred relative abundance

of $C^{18}O$ in Chamaeleon is smaller by about 20%. Using the Kainulainen et al. (2006) relationship, we find a peak H_2 column density of 1.5×10^{22} cm^{-2}. This peak column density corresponds to a visual extinction $A_V = 16$ mag, which is reasonably consistent with the lower limit of $A_V > 19$ mag found from near-infrared star counts by Kainulainen et al. (2006).

The H_2 column density distribution is displayed in the bottom left panel of Figure 1. The column density distribution looks largely similar to the $C^{18}O$ intensity map because we assumed a constant excitation temperature and most of the emission has small optical depth. If we assume a smaller excitation temperature of 8 K, the peak column density increases by 12% to 1.7×10^{22} cm^{-2}, but the emission is still largely optically thin, and the resulting column density map still looks very much like the integrated intensity map.

3.2. N_2H^+ Observations

N_2H^+ ($J = 1 \rightarrow 0$) emission is divided into seven hyperfine components due to the interaction between the molecular magnetic moment and the magnetic moments of the two nitrogen nuclei. The seven components are distributed unevenly in frequency, with one high frequency component separated from the main triplet by nearly 3 MHz (8 km s^{-1}), and a low frequency triplet of components separated from the main triplet by approximately 2 MHz (6 km s^{-1}). The components within each triplet have separations of ~200 kHz (0.6 km s^{-1}).

The hyperfine splitting presents an opportunity to deduce the optical depth of the N_2H^+ emission from the relative intensities of the hyperfine components, since under thermal equilibrium conditions, each component should carry a well-defined fraction of the total ($J = 1 \rightarrow 0$) optical depth. In principle, one should fit the relative intensities of all seven components to determine the optical depth; however, Caselli et al. (1995), Daniel et al. (2006), and Daniel et al. (2007) note that for most N_2H^+ sources, several of the components appear to have anomalous relative intensities which are not consistent with a single excitation temperature model for the emission. In particular the $F_1, F = 1,0 \rightarrow 1,1$, and $1,2 \rightarrow 1,2$ components show the largest excitation anomalies. Because of these anomalies, fitting a single-temperature model to all seven results in a poor fit to the spectrum and an overestimate of the total N_2H^+ ($J = 1 \rightarrow 0$) optical depth (Daniel et al. 2007).

These two anomalous components reside in the lowest frequency triplet of the N_2H^+ ($J = 1 \rightarrow 0$) spectrum, which is separated by approximately 2 MHz (5 km s^{-1}) from the main triplet of components. To avoid biasing our optical depth estimates by this known anomaly, we chose to use the emission from only the main triplet and the isolated high frequency component. Using the "HFS" routine in CLASS, we compared the relative intensities of these components with that expected from thermal equilibrium conditions to determine the optical depth in each component. We then calculated a total optical depth in the ($J = 1 \rightarrow 0$) transition by adding these optical depths and correcting the sum for the one-third of the total optical depth that should be associated with the low frequency triplet (assuming a thermal equilibrium partition of optical depth). See Appendix A for more details on this procedure.

We measured a total optical depth (that is, the total optical depth of an equivalent unsplit line) at each position in the N_2H^+ map. Total optical depths ranged from 1.5 to 15 with a typical uncertainty of 1–1.5. With the measured optical depth and the peak main-beam temperature, we calculated the excitation temperature, assuming that the emission filled the 49″ beam with a constant excitation temperature. We found excitation temperatures ranging from 4.5 to 8.4 K using this technique. These values are smaller than the kinetic temperature determined from NH_3 measurements (Tennekes et al. 2006), indicating either that the N_2H^+ emission arises from a cooler dense gas component or that the N_2H^+ is not fully thermalized. Large velocity gradient calculations by Daniel et al. (2006) show N_2H^+ ($J = 1 \rightarrow 0$) excitation temperatures in this range for a kinetic temperature of 10 K and volume densities of $\sim 10^5$ cm^{-3}.

For several positions in the map, the signal-to-noise ratio was insufficient to produce a well-constrained estimate of the optical depth. For those positions where the uncertainty in tau was greater than one-quarter the derived value, we used a different technique to estimate the optical depth. We assumed that the excitation temperature at each of these points was 5 K and then calculated the total optical depth from a comparison between the assumed excitation temperature and the peak main-beam antenna temperatures. We chose this value for the assumed excitation temperature based on examination of well-fit data, with a bias toward the weaker lines, since these lines are most similar to the spectra with unconstrained optical depths.

Using the excitation temperature, the total optical depth, and the measured line width, we calculate the total N_2H^+ column density in the $J = 1$ rotational energy level at each map position, and then by assuming thermalized energy levels, we calculate the total N_2H^+ column density. These values were converted to an equivalent H_2 column density using an assumed abundance ratio $[N_2H^+]/[H_2] = 3 \times 10^{-10}$, the mean value found by Caselli et al. (2002), based on a study of some 60 nearby dense cores, though none were in the Chamaeleon clouds. Kontinen et al. (2000), Tennekes et al. (2006), and Belloche et al. (2006) have measured the N_2H^+ abundance toward the MMS-1 source; however, the values determined—$[N_2H^+]/[H_2] = 10 \times 10^{-10}$ (Kontinen et al. 2000), 5×10^{-10} (Tennekes et al. 2006), and 2.2×10^{-10} (Belloche et al. 2006)—vary by a factor of five and bracket the Caselli et al. (2002) mean value. Recently, Johnstone et al. (2010) have measured $[NH_3]/[N_2H^+] = 22 \pm 10$ for sources in the Perseus cloud. Assuming $[NH_3]/[H_2] = 10^{-8}$, they conclude $[N_2H^+]/[H_2] = 4.5 \times 10^{-10}$. For this work, we use the Caselli et al. (2002) value mainly because it is in the middle of the other measured values, but recognize that the uncertainty in this mean value is a factor of two or more and that the core-to-core variation in this abundance ratio might also be a factor of two. Using this technique, we find a total mass in the mapped area of $13 \pm 3\ M_\odot$. This value is consistent with the mass of $15\ M_\odot$ found by Kontinen et al. (2000) for the "ridge" of dust emission mapped at 200 μm.

The column density map inferred from the N_2H^+ observations is displayed in the bottom right panel of Figure 1. The map consists of a core of high column density colocated with MMS-1 and a more extended distribution of lower column density that extends to the northeast past the positions of IRS 4 and IRS 11. The map looks qualitatively similar to the intensity map, though the contrast between the high column density region around MMS-1 and the lower column density portions of the map is greater than the contrast between bright and fainter emission in the integrated intensity map because of the large optical depth of the emission toward MMS-1.

The peak column density inferred from the N_2H^+ observations is 8.5×10^{22} cm^{-2}—more than five times that inferred from the $C^{18}O$ measurements. A comparison between the column

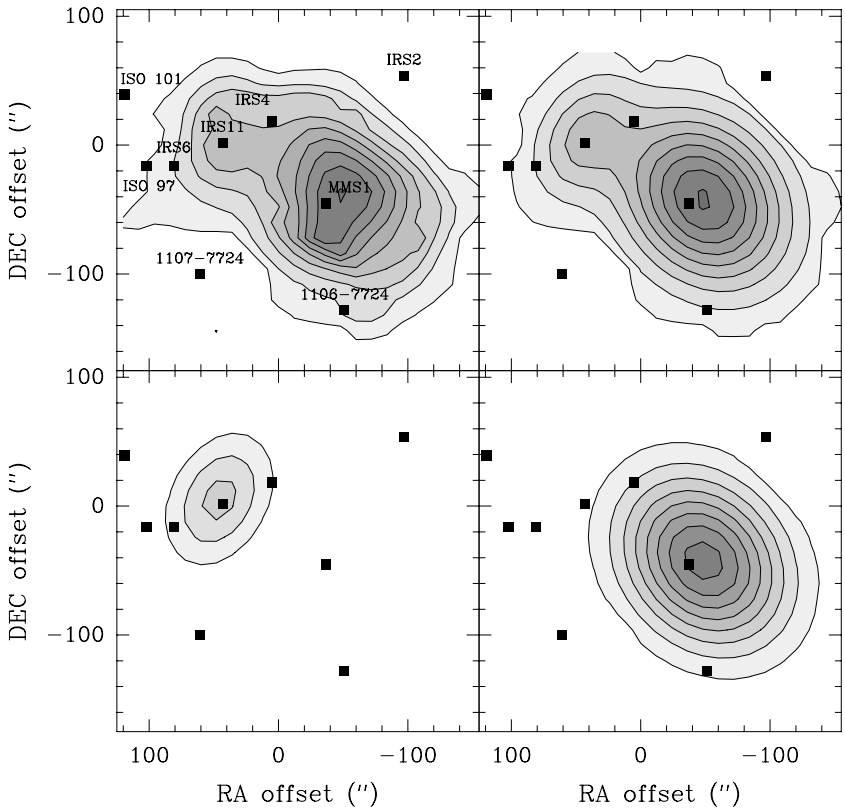

Figure 2. Upper left: inferred H_2 column density from measured N_2H^+ column density toward the Ced 110 region. YSOs are labeled as in Figure 1. Upper right: best-fit model containing two Gaussian blobs and a flat background (see the text for details). Lower left: first fitted Gaussian component. Lower right: second fitted Gaussian component. In all panels, contours begin at 8.5×10^{21} cm^{-2} and increment by 8.5×10^{21} cm^{-2}.

Table 1
Gaussian-fit Parameters for Column Density Map

Core	*x*-pos. (″)	*y*-pos. (″)	Peak $N(H_2)$ (10^{21} cm^{-2})	Major Axis (″)	Minor Axis (″)	P.A. (deg)
IRS 11	46(3)	5(3)	29(3)	81(8)	55(6)	−28(9)
MMS-1	−49(1)	−42(1)	72(2)	113(5)	90(4)	40(5)

Table 2
Core Masses

Core	Model Mass ($M_\odot$)	R_{core} (pc)	$\bar{n}$ (10^5 cm^{-3})	α	Background Mass ($M_\odot$)
IRS 11	1.6(3)	0.035(4)	2.1(3)	1.4(3)	2.4(9)
MMS-1	9.3(7)	0.068(3)	2.4(1)	0.5(1)	

density maps derived from the $C^{18}O$ and N_2H^+ data shows $C^{18}O$ observations to be almost completely insensitive to the dense gas seen in N_2H^+. This discrepancy is commonly seen toward dense cores in regions of low-mass star formation and is usually explained by invoking depletion of CO onto dust grains (see, e.g., Caselli et al. 1999; Bacmann et al. 2002; Bergin et al. 2002). The depletion factor, found here, 5.7 ± 2, is smaller than that typically found toward starless cores (Crapsi et al. 2005), but nonetheless indicates that a substantial column of CO has frozen out onto dust grains. Such depletion is expected given the low excitation temperatures determined from the N_2H^+ measurements.

The ridge of high column density in this region extends from southwest to northeast, with a pronounced enhancement toward the southwest end coincident with MMS-1. The spatial distribution is not well described by a simple single structure, so we modeled the distribution with two Gaussian "cores" and a flat background. Each Gaussian core was characterized by a center position, peak column density at the center position, FWHM major and minor axes, and a position angle for the major axis. Thus, the model contained 13 independent parameters. The best-fit values and uncertainties for each parameter were found via the chi-square minimization routine "NonlinearModelFit" in *Mathematica* (Wolfram Research, Inc. 2008). The fitting process starts from an initial "guess" for the positions, sizes, and orientations of the cores. Several different initial configurations were tried, including configurations involving nested structures (i.e., a small high column density core superimposed on an extended low column density structure); in all cases, the models converged to the best-fit result were presented in Figure 2 and in Tables 1 and 2. The 1σ statistical uncertainty in each parameter in the Tables is listed in parentheses after each value.

The best-fit model consists of two nearly spatially distinct cores of quite unequal mass. The larger core has FWHM size of 0.09×0.07 pc, a total mass of $9.3 \pm 0.6\ M_\odot$, and is centered 12″ from the position of MMS-1. The smaller core has an FWHM size of 0.06×0.04 pc, a mass of $1.6 \pm 0.3\ M_\odot$, and is centered 4″ from the position of IRS 11. The model allocates $2.4\ M_\odot$ (20% of the total measured mass) to the flat background. Though this type of decomposition can be very easily overinterpreted, it does suggest that the mass available to the trio of Class I systems—IRS 6, IRS 11, and IRS 4—is a small fraction of the total mass in the region.

Belloche et al. (2011) found similar structures in their decomposition of 870 μm continuum emission. Using the *Gaussclumps* algorithm, they identified emission associated

with IRS 4 (their source S4 with a mass of 0.18 $M_\odot$) and assigned the remainder of the emission in the region to clumps designated as starless or harboring a Class 0 source (sources labeled as "C"). Sources C1 and C3, the most massive of these clumps, are positionally coincident with the two cores identified in our decomposition of the N_2H^+-derived H_2 column density. Their Source C3, which we identify with the N_2H^+ core near IRS 11, has a mass of 1.2 $M_\odot$, 75% of the mass we find for the core. Belloche et al. (2011) find a mass of only 3.4 $M_\odot$ for Source C1, which is coincident with our larger, 9.3 $M_\odot$ core. The discrepancy here, a factor of 2.4, may be due to the smaller size of Source C1. The *Gaussclumps* algorithm appears to have broken the structure we identify in our data into two structures (C1 and C2) in the 870 μm map; the combined mass from these two structures is 5 $M_\odot$, more than 50% of the mass we find.[7] Thus while the spatial distribution of the structures found here and in Belloche et al. (2011) is quite similar, the masses found by Belloche et al. (2011) are systematically lower. This discrepancy could easily be resolved if the N_2H^+ abundance ratio were increased to $[N_2H^+]/[H_2] = 5 \times 10^{-10}$, a value favored by Tennekes et al. (2006), or if the dust opacity used by Belloche et al. (2011) were decreased by a similar factor.

3.2.1. Virial Parameters

With an estimate for the velocity dispersion of the dense material, we can calculate its virial mass. We determine the nonthermal velocity dispersion (σ_{NT}) by subtracting the N_2H^+ thermal velocity dispersion (determined from the measured excitation temperature) in quadrature from the observed velocity dispersion (σ_{meas}),

$$\sigma_{nt}^2 = \sigma_{meas}^2 - \frac{kT_x}{m_{N_2H^+}}. \quad (1)$$

The total velocity dispersion (σ_{TOT}) for the material is then equal to the quadrature sum of the nonthermal velocity dispersion from above and the thermal velocity dispersion for a molecule of mean mass,

$$\sigma_{tot}^2 = \sigma_{nt}^2 + \frac{kT_x}{2.3m_H}. \quad (2)$$

For each core, we use the excitation temperature and velocity dispersion determined from the spectrum nearest the core's center position. The virial mass for a constant density sphere is then

$$M_v = \frac{9}{2}\frac{\sigma_{tot}^2 R_{core}}{G}. \quad (3)$$

The radius R_{core} is determined from the Gaussian fits to the observed column density distribution, deconvolved to remove the smearing effects of the telescope beam. The prefactor $\frac{9}{2}$ differs from the more standard value (5), because we assume the core to have a Gaussian density profile. See Appendix B for further discussion.

The virial parameter α is the ratio of the virial mass to the model core mass, $\alpha = \frac{M_v}{M_{model}}$, and gives a measure of the extent to which motions in the core might support it against gravitational collapse. We also calculate the mean density $\overline{n}$ for each clump as

$$\overline{n} = \frac{N_{max}}{2R_{core}}, \quad (4)$$

where N_{max} is the peak column density from the least-squares fit. The measured mass, radius, virial parameter, and mean density for each core are listed in Table 2, along with their statistical uncertainties determined from propagation of the statistical uncertainties in each input parameter in the relationships above.

The smaller core has an average density of 2.1×10^5 cm^{-3}, a value comparable to but larger than the critical density for the N_2H^+ ($J = 1 \rightarrow 0$) transition. The mass of the core is almost certainly larger than that of IRS 11, the source most closely colocated with the core, and quite possibly larger than the sum of the masses of IRS 11, IRS 4, and IRS 6, given their low luminosities (Lehtinen et al. 2001). With $\alpha = 1.4 \pm 0.3$ the core is very nearly in virial equilibrium. If IRS 11 is located at the center of this core, then this value for α is an upper limit.

The larger core has $\alpha = 0.5 \pm 0.1$ and in the absence of any other support mechanisms it is unstable against gravitational collapse. It is perhaps not surprising, then, that MMS-1 is projected against the center of this mass distribution. With a $T_{bol} = 20$ K and a spectral energy distribution (SED) peaking in the far-infrared and undetected at wavelengths smaller than 24 μm, it is virtually certain that MMS-1 is embedded near the center of this core, where the beam-averaged column density is greater than 90 A_V. The core's large mass and small α also suggest that this structure may be susceptible to fragmentation (Tsuribe & Inutsuka 1999). Its location in the middle of a small grouping of YSOs suggests a history of fragmentation on larger scales, and the current properties of the remaining dense gas indicate that such fragmentation may also occur in the future.

3.3. ^{12}CO Observations

Figure 3 shows the blueshifted ^{12}CO ($J = 3 \rightarrow 2$) and ($J = 1 \rightarrow 0$) emission toward this region. The ^{12}CO ($J = 3 \rightarrow 2$) data (top left panel) are reproduced from Hiramatsu et al. (2007), while the ($J = 1 \rightarrow 0$) data (top right panel) show our new data. Both datacubes were integrated over the velocity range $-4 < V_{LSR} < 3$ km s^{-1} to produce these plots. The line center velocities for the C^{18}O and N_2H^+ emission are $V_{LSR} \sim 4.4$ km s^{-1}, so this ^{12}CO emission is blueshifted by 1.5–8.5 km s^{-1}. The maps show a pronounced peak between MMS-1 and the Class I embedded source IRS 4, with a 2′ (∼0.1 pc) extension to the southeast.

The blueshifted ^{12}CO ($J = 1 \rightarrow 0$) emission extends along a NW–SE axis positioned between the Class I sources IRS 4, IRS 11, and IRS 6 to the northeast, and the Class 0 source MMS-1 and its associated N_2H^+ emission to the southwest. The strongest emission is located on a line between IRS 4 and MMS-1, approximately 30″ (∼5000 AU in projection) to the southwest of IRS 4.

The blueshifted lobe has a spatial structure very similar to that found by Hiramatsu et al. (2007) in ^{12}CO ($J = 3 \rightarrow 2$) over the same velocity range. They also detect a very weak and nearly pointlike redshifted component coincident with IRS 4. We do not detect a localized redshifted lobe at the position of IRS 4 in our ^{12}CO ($J = 1 \rightarrow 0$) data, although the ^{12}CO ($J = 1 \rightarrow 0$) line is very broad at the position of IRS 4. The red wing emission at this position is not sufficiently velocity-shifted to distinguish it from ambient cloud emission at other positions. It is likely that by using the higher ^{12}CO transition, Hiramatsu et al. (2007) were able to better discriminate the redshifted outflow emission from the lower excitation ambient gas.

Based on the spatial distribution of both velocity-shifted lobes, Hiramatsu et al. (2007) identify IRS 4 as the driving source for this outflow, in agreement with most previous

[7] Belloche et al. (2011) identify only one other structure in this region. Source C14, with a mass of 0.21 $M_\odot$, might be associated with ISO 97, as its center lies 13″ south of that source's position.

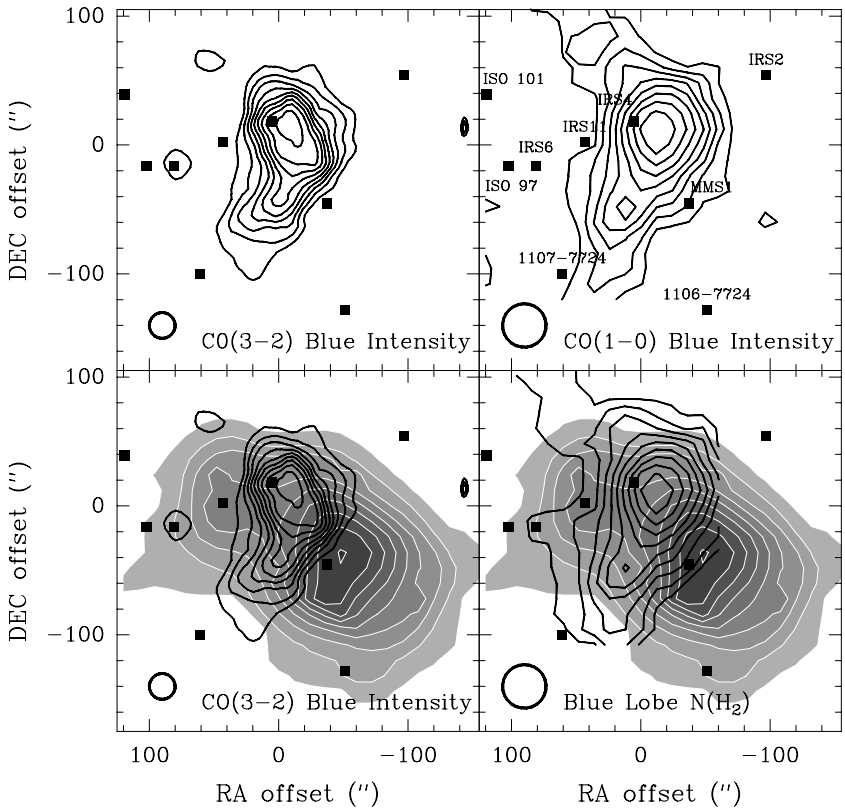

Figure 3. Blueshifted ^{12}CO outflow emission from IRS 4 in the ($J = 3\rightarrow2$) (top left panel) and ($J = 1\rightarrow0$) (top right panel) transitions. The ^{12}CO ($J = 3\rightarrow2$) data are reproduced from Hiramatsu et al. (2007). In both panels, the CO emission is integrated over the velocity range $-4 < V_{LSR} < 3$ km s^{-1}, and contours run from 20% of peak integrated intensity to 90% in increments of 10%. The peak integrated intensity is 5.0 K km s^{-1} in the ($J = 3\rightarrow2$) data and 6.7 K in the ($J = 1\rightarrow0$) data. Bottom left panel: the blueshifted ^{12}CO ($J = 3\rightarrow2$) emission plotted over the dense gas column density determined from the N_2H^+ data (filled contours). Dense gas contours are as in Figure 1. Bottom right panel: the total H_2 column density in the blue lobe of the ^{12}CO outflow determined from a comparison between the ($J = 3\rightarrow2$) and ($J = 1\rightarrow0$) emission (black contours), plotted over the dense gas column density. The outflow lobe contours start at 1×10^{19} cm^{-2} and increment by 5×10^{18} cm^{-2}.

studies (Mattila et al. 1989; Prusti et al. 1991; Belloche et al. 2006). However, the picture is complicated by the presence of Herbig–Haro objects HH 49 and 50, which lie approximately 0.5 pc to the south, along a line with position angle 192° (east of north); the proper motion and Doppler velocities of these objects indicate that they are moving away from the Ced 110 region with velocities of ∼100–300 km s^{-1} along a line inclined ∼12° *redward* from the plane of the sky (Schwartz & Dopita 1980; Schwartz et al. 1984). The presence of both blueshifted ^{12}CO emission and redshifted HH objects to the south of IRS 4 led Bally et al. (2006) to reject IRS 4 as the driving source, and instead to propose MMS-1 as the outflow driver, since this source lies between the blueshifted ^{12}CO and the redshifted HH objects. Our ^{12}CO maps extend 100″ south of MMS-1, but we find no localized redshifted gas in this region to support this contention.

We contend that IRS 4 is the driving source for both the observed ^{12}CO outflow and the HH objects. High-resolution near- and mid-infrared images show this source to be embedded in a bowtie-shaped reflection nebula, which has been modeled as an embedded star–disk system whose axis is oriented 70° ± 5° with respect to the line of sight (Pontoppidan & Dullemond 2005). An outflow jet oriented along this axis could excite the HH 49/50 system and produce the measured space velocities for these objects. With an outflow jet directed redward to the south of IRS 4, it is difficult to explain the presence of blueshifted ^{12}CO emission; however, in Section 4.2.1 below we discuss how interactions between the outflow and dense gas might produce the observed blueshifted ^{12}CO flow.

3.3.1. Column Density and Mass of the Blueshifted Gas

We calculate the column density and mass of the blueshifted emission by comparing our data with the ^{12}CO ($J = 3\rightarrow2$) data from Hiramatsu et al. (2007). We first convolved the ^{12}CO ($J = 3\rightarrow2$) data to the spatial resolution and sampling of the ^{12}CO ($J = 1\rightarrow0$) data set using a Gaussian kernel. We then modeled the integrated intensity in both transitions, assuming LTE conditions, and varied the input excitation temperature and total ^{12}CO column density to match the observations at each position. We converted the ^{12}CO column density to an equivalent H_2 column density assuming $[CO]/[H_2] = 10^{-4}$. The column density map is shown in the bottom right panel of Figure 3. The column density distribution looks quite similar to the ^{12}CO ($J = 1\rightarrow0$) integrated intensity distribution because the excitation temperatures vary little over the lobe and inferred optical depths are generally small. The excitation temperature over the lobe ranges from 6.4 K to 10.6 K, with an average value of 8 K.

The total mass in the blueshifted lobe, 4.4×10^{-3} $M_\odot$, is very small compared to the masses of outflows from other Class I sources (Wu et al. 2004). However, since the outflow appears to be nearly in the plane of the sky, it is very likely that a large fraction of the outflowing gas is not sufficiently Doppler shifted along our line of sight to distinguish it from ambient cloud material. In addition, it is possible that, except in the region near the MMS-1 dense core, the outflow does not interact strongly with molecular material. Extinction maps indicate that the cloud column density decreases rapidly to the south of this region, and the fact that redshifted HH objects HH 49 and 50 can be detected

optically suggest that there is little obscuring molecular cloud material along the outflow's southern path.

4. DISCUSSION

Though the Chamaeleon I complex is better known for its scattered and isolated star formation, the Ced 110 region is relatively dense and rich in forming stars. Using the definition presented by Bressert et al. (2010), MMS-1 lies in a region with YSO surface density $\Sigma_{\rm YSO} = 157$ pc^{-2}, a value considerably larger than the mean YSO surface density of 22 pc^{-2} for all forming stars within 500 pc (Bressert et al. 2010). Thus, the region has been a site of closely spaced multiple star formation in the recent past, and based on the observations presented here, has the capacity to continue to produce stars. Furthermore, the high density of YSOs appears to be influencing the structure of the dense gas, even though each of the forming stars is of low luminosity and mass.

4.1. The Spatial Distribution of Dense Gas and YSOs

The dense gas is more centrally concentrated than the YSO distribution, with most of the mass contained in the core immediately surrounding MMS-1. An area of lower column density material extends to the northeast encompassing the positions of IRS 4 and 11. To the east, IRS 6 sits on the edge of this extension. The other sources in this region, all of which have Class II or later classifications, are located in regions of very low dense gas column density. IRS 2 in particular is clearly separate from the dense gas, as it illuminates the dense gas region from the outside, producing a bright optical reflection nebula.

The dense gas column density at the positions of each of the forming stars anticorrelates with the forming star's $T_{\rm bol}$. The bolometric temperature, a measure of the SED and an indicator of evolutionary stage, is largely determined by the line-of-sight extinction to the forming star or star/disk system for deeply embedded sources. The column density determined from N_2H^+ emission, on the other hand, is a beam-averaged measurement of the mass available to the forming star. The relationship between these two quantities might arise naturally if these stars formed in their current positions from dense cores that have already dissipated or are in the process of dissipating. If instead, these stars formed elsewhere (say, near the center of the existing dense core) and then migrated to their current positions, it would be difficult to explain why the least evolved sources preferentially moved in the direction of the extended dense core material. Thus, we conclude that these youngest stars probably have formed at or near their current positions and that the dense core material seen today is the "remnant" from a more spatially extended distribution of dense gas.

This line of reasoning suggests that recent star formation has progressed from northeast to southwest in this region. The flat spectrum sources ISO 97 and IRS 6 appear to be at a later evolutionary state than the more embedded sources IRS 11 and 4, and certainly older than the very young source MMS-1. It also appears that the dense cores out of which ISO 97 and IRS 6 formed are no longer present, while IRS 11 and perhaps IRS 4 still have access to a dense gas reservoir. MMS-1, with its Class 0 SED and its position projected against the center of the massive dense core, is almost certainly actively accreting dense gas. This implies that the time required for a dense core to dissipate is comparable to the time required for a forming star to reach the flat spectrum stage. Based on population studies of low-mass YSOs, the Class I/Flat timescale is approximately 6–9 $\times 10^5$ yr (Evans et al. 2009) or about two or three times crossing times for a typical 1 $M_\odot$ dense core.

IRS 11 appears to be the youngest of the four sources in this region, based on the shape of its SED. ISO 97 and IRS 6 have substantially flatter spectral slopes through the mid-infrared, and though IRS 4 has a comparably steep mid-infrared slope, its bowtie-shaped near-infrared nebulosity strongly indicates that it is an edge-on system. Edge-on systems often produce SEDs which belie their true ages, making them appear younger than they really are (Robitaille et al. 2006).

It is interesting, then, that the decomposition of the N_2H^+ emission into two Gaussian cores nearly centered the northeastern core on the position of IRS 11. If this dense gas were associated *only* with IRS 11, then the cores that produced not only ISO 97 and IRS 6, but also IRS 4, may have already dissipated. Pontoppidan & Dullemond (2005) have modeled the near-infrared emission from IRS 4 as a star–disk system embedded within an overlying envelope and determined the extinction to the star/disk system (but not including the extinction associated with the disk) corresponds to $A_{\rm J} = 3.3$ mag. This value implies an overlying column density of $\sim 10^{22}$ cm^{-2}—approximately one-fourth of the total beam-averaged dense gas column density along this line of sight. Therefore, the bulk of the column density in this region might not be associated with IRS 4, but instead with the spatially extended dense cores around IRS 11 and MMS-1. This suggests that dense core dissipation might proceed even more swiftly, perhaps on the timescale associated with just the Class I phase, about 5×10^5 yr (Evans et al. 2009). However, it must be noted that this speculation depends sensitively on the Gaussian decomposition and must be confirmed with higher spatial resolution measurements.

There is some evidence that the dense gas in the northeastern extension is dissipating. The decomposition of the N_2H^+ data into two Gaussian structures produces a core centered on the position of IRS 11 whose virial parameter α is larger than that for the MMS-1 core, suggesting that it is less gravitationally bound than the more massive structure to the southwest. The column density of dense gas in the IRS 11 region is lower than that toward MMS-1, and the depletion factor, measured as the ratio of H_2 column density determined from N_2H^+ measurements to the H_2 column density determined from $C^{18}O$ measurements, is also lower. At the position of MMS-1, the depletion factor is 5.7 ± 2, while in the northeastern extension, the depletion factor is typically three. A smaller depletion factor may indicate that more of the dense gas has been stirred up, liberating frozen CO from grain surfaces, or that a larger fraction of the line of sight is dominated by lower density material. Additionally, the FWHM line width of the $C^{18}O$ emission is approximately 20% larger in this region than toward the MMS-1 core ($\Delta v_{\rm FHWM} \sim 0.6$ km s^{-1} versus 0.5 km s^{-1}), suggesting that this lower density material may have been stirred by the forming stars; however, the FWHM line width of the N_2H^+ emission in this extension is not significantly larger than that toward the MMS-1 core.

4.2. The MMS-1 Dense Core

Most of the dense gas in this region is confined to the dense core associated with MMS-1. The total mass associated with this core, based on the Gaussian decomposition, is $9.3 \pm 0.6\ M_\odot$—much larger than the masses of the stars that have formed in this region. Therefore, even though this core is associated with only one forming star, it is extremely unlikely that MMS-1 will accrete all, or even a large fraction of the core

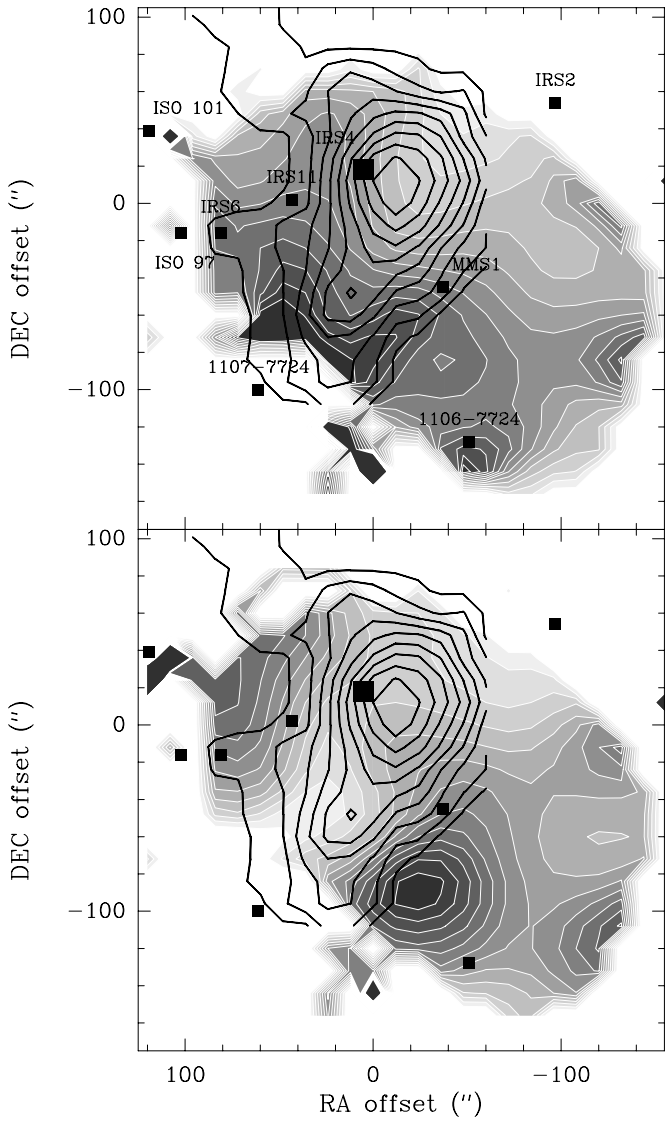

Figure 4. Top panel: the blueshifted lobe of the CO outflow (black contours) plotted over the measured N_2H^+ FWHM line width (filled contours). The outflow lobe contours start at 1×10^{19} cm^{-2} and increment by 5×10^{18} cm^{-2}. The line width contours start at 0.32 km s^{-1} and increment by 0.03 km s^{-1}. Larger line widths correspond to darker colors in the gray scale. Bottom panel: the blueshifted lobe of the CO outflow (black contours) plotted over V_{LSR} measured from the N_2H^+ spectra (filled contours). V_{LSR} contours begin at 4.24 km s^{-1} and increment by 0.02 km s^{-1}. Larger velocities correspond to darker colors in this gray scale. The filled squares mark the positions of the YSOs as in Figure 1. The square marking IRS 4, the driver of the outflow, is enlarged in these panels.

mass. Rather, our virial analysis suggests that it is susceptible to fragmentation and therefore may have the capacity to produce several stars. Such multiple star formation in the future would be consistent with the recent past in this region, where several YSOs have formed over the last 1 Myr.

4.2.1. External Interactions with the MMS-1 Dense Core. I. The IRS 4 Outflow

The recent star formation activity appears to be affecting the MMS-1 dense core. Both the outflow from IRS 4 and the luminosity from IRS 2 have produced observable impacts on the core material. Below we discuss these external interactions on the dense core material.

There is strong evidence that the outflow from IRS 4 is interacting with the MMS-1 dense core. The blue outflow lobe extends initially southwestward from IRS 4, but then turns sharply to the southeast just northeast of the peak of the MMS-1 dense core (see the bottom left panel of Figure 3 which shows the ^{12}CO ($J = 3 \rightarrow 2$) outflow superimposed over the dense gas column density determined from the N_2H^+ observations). The blue lobe then extends southeastward parallel to, but just northeast of, the high column density ridge seen in N_2H^+. This part of the blue lobe appears to run between the MMS-1 dense core and the northeast extension potentially associated with IRS 11. The highest velocity ^{12}CO emission in the blue lobe is found at the position of the abrupt shift in direction. The morphology and dynamics strongly suggest that this outflowing gas is interacting with the dense core associated with MMS-1. However, there is no strong evidence in the N_2H^+ data of any such interaction at the point where the outflow turns sharply. The N_2H^+ line width at this point is among the smallest observed (see Figure 4 top panel).

Broader N_2H^+ lines are found farther to the southeast along and particularly at the edges and the "head" of the CO outflow, indicating a working surface between the faster moving low density gas and the dense surroundings. The N_2H^+ FWHM line widths range from $\Delta V_{meas} = 0.35$ km s^{-1} in the northwest to 0.65 km s^{-1} at the head of the outflow lobe. The increase in line width is significant in that the quiescent gas is dominated by thermal motions, while the dense gas near the head of the outflow lobe is dominated by nonthermal motions. Moreover, the N_2H^+ line center velocities appear to be shifted to the blue in the "channel" through which the ^{12}CO outflow lobe passes (See Figure 4, bottom panel). The morphology and energetics in this region suggest a more direct interaction between the outflow and dense gas—one where the flow is carving into the dense material, stirring it up, and perhaps actively dissipating it.

While it is plausible that an outflow can inject energy into a dense core, it is difficult to understand how it could be redirected by the dense core, as it appears to be in the region between IRS 4 and MMS-1. The ram pressure exerted by an outflow can be expressed as

$$P_{\rm flow} = \rho_{\rm flow}\, v_{\rm flow}^2 = 3500 \left(\frac{n_{\rm flow}}{1000\,{\rm cm^{-3}}}\right)\left(\frac{v_{\rm flow}}{30\,{\rm km\,s^{-1}}}\right)^2 {\rm pPa}, \quad (5)$$

where $\rho_{\rm flow}$, $v_{\rm flow}$, and $n_{\rm flow}$ are the mass density, velocity, and number density of the outflowing gas. For reasonable low-mass outflow parameters, this ram pressure is more than two orders of magnitude greater than the thermal pressure of the dense core,

$$P_{\rm th,core} = n_{\rm core}\, kT_{\rm core} = 11 \left(\frac{n_{\rm core}}{10^5\,{\rm cm^{-3}}}\right)\left(\frac{T_{\rm core}}{8\ K}\right) {\rm pPa}, \quad (6)$$

where $n_{\rm core}$ and $T_{\rm core}$ are the number density and kinetic temperature of the dense core material. Our observations of the nonthermal component of the N_2H^+ line widths indicate that additional pressure support due to small-scale turbulent motions will be at most comparable to $P_{\rm th,core}$, and, unless the magnetic field is substantially stronger than is typical for low-mass star formation regions, any magnetic pressure will also be similar in strength. Therefore, one should expect the outflow to bore through the core without difficulty, and yet the observations indicate that the outflow is deflected.

It is possible that the outflowing gas is moving more slowly than we have assumed, but given the measured line-of-sight blueshift of $\sim$3 km s^{-1} and the nearly plane of the sky orientation

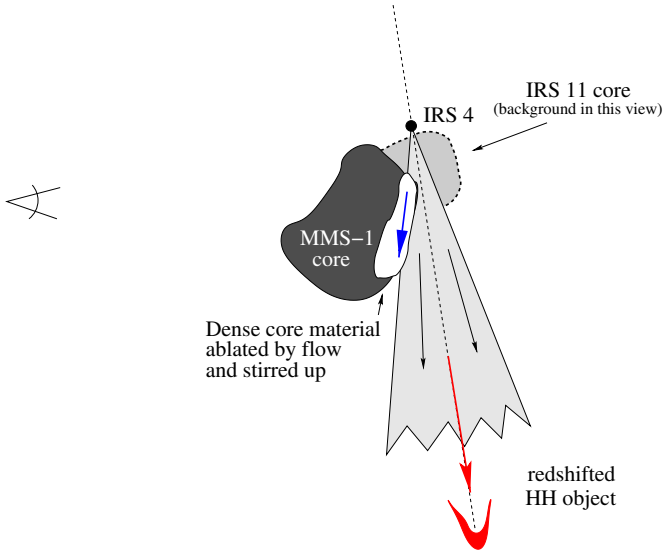

Figure 5. Side-view sketch indicating the possible spatial relationship between IRS 4, its outflow, and the MMS-1 dense core. The redward-directed jet, which drives the observed HH objects 49 and 50, lies at the center of a broader outflow wind. The near edge of the outflow wind is blueshifted with respect to the line of sight and interacts with the far side of the MMS-1 dense core, producing the observed blueshifted ^{12}CO outflow and the broader line widths in the dense gas.

(A color version of this figure is available in the online journal.)

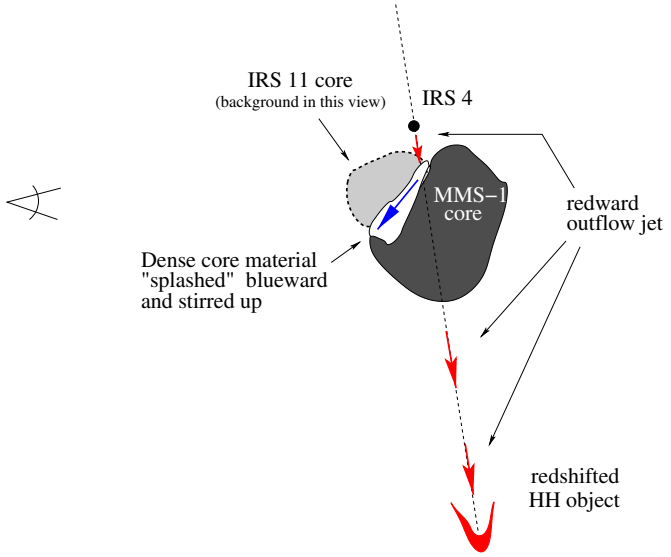

Figure 6. Side-view sketch indicating the possible spatial relationship between IRS 4, its outflow, and the MMS-1 dense core. The redward-directed jet drives the observed HH objects 49 and 50, but may not be detectable in ^{12}CO because it is nearly in the plane of the sky and does not interact with dense gas except in the vicinity of the MMS-1 dense core. The interaction between the jet and the MMS-1 dense core may produce the blueshifted "splash" of material detected as blueshifted ^{12}CO emission and responsible for broadening the N_2H^+ lines in the southeastern portion of the MMS-1 dense core.

(A color version of this figure is available in the online journal.)

for the outflow, it seems very unlikely that the outflowing gas has a space velocity less than 10 km s^{-1}, and even with $v_{\rm flow}$ = 10 km s^{-1}, the ram pressure of the outflow is still an order of magnitude larger than the internal pressure of the dense core material. Another more plausible explanation is that the outflow does not impact the core directly, but instead delivers a glancing blow. At a large angle of incidence $\Theta_{\rm inc}$, the ram pressure across the core/outflow interface would be reduced by a factor of $\cos^2(\Theta_{\rm inc})$ and for sufficiently large angles, the core would be able to withstand the outflow's ram pressure and even redirect some of the flow. This type of interaction requires only that the MMS-1 core be slightly displaced from the outflow axis, either foreground or background to the outflow along our line of sight.

A possible geometry with the MMS-1 core foreground to the jet axis is shown in Figure 5. Here we assume that the outflow jet lies at the center of a broader outflow wind with an opening angle larger than 12° so that the near side of the outflow cone is blueshifted with respect to the line of sight. Opening angles of 20°–40° are common for molecular outflows from very young sources (Arce & Sargent 2006), and the blueshifted CO emission seen south of IRS 4 could arise from the interaction between the near side of the outflow and the foreground MMS-1 dense core. The interaction could take place at a large angle of incidence, and the dense core material might be able to redirect a portion of the outflow, producing the observed kink. In addition, the ablation of the outflow into the outer part of the dense core could produce the observed broader N_2H^+ line widths and slight blueward shifts in N_2H^+ linecenter velocities. The lack of observed redshifted ^{12}CO emission to the south of IRS 4 is puzzling, but it could be explained if the rest of the outflow cone interacts with very little dense gas.

Alternatively, Figure 6 depicts a geometry where the MMS-1 core is slightly background to IRS 4 and more directly impacted by the outflow jet. The interaction between the jet and core produces a "splash" of dense material directed away from the jet axis and along the foreground edge of the dense core. This putative configuration is somewhat similar to the geometry associated with the "bent" HH 270/110 optical jet emanating from the 5 $L_\odot$ Class I source IRAS 05489+0256. Reipurth et al. (1996) suggested that this jet changes direction due to an interaction with a dense core. Sepulveda et al. (2011) mapped the dense gas in the region and found the dense core which may be responsible for the deflection. Raga et al. (2002) modeled such an interaction between jet and dense core and found that some portion of the jet (along with ablated dense core material) can be deflected into a flow directed away from the jet axis by an angle of ∼30°. The outflow detected in this work may be the result of a similar interaction between an unseen jet and the MMS-1 dense core. The observed blueshifted ^{12}CO emission might then be produced by the portion of the jet and core material "splashed" into our line of sight by the interaction. If this splashed material were to run along the foreground edge of the MMS-1 dense core, it might carve a channel of broader N_2H^+ line widths as is observed. However, this geometry also requires that the jet pierce the dense core in order to drive HH objects 49 and 50; there is no evidence in the N_2H^+ data for such an interaction through the bulk of the dense core.

4.2.2. External Interactions with the MMS-1 Dense Core. II. Influence from IRS 2?

There is some evidence that the measured N_2H^+ excitation temperature increases at the position of the kink in the blue outflow. On the northwest side of the outflow lobe, the measured excitation temperature rises from ∼5 K to a peak of 8.3 K along a ridge of high excitation temperature material that extends to the southwest. However, this ridge does not follow the outflow lobe as it turns to the southeast; rather, there is a misalignment between high T_x N_2H^+ gas and the outflow lobe, with the ridge of high T_x gas displaced to the west, running along the western edge of the dense core.

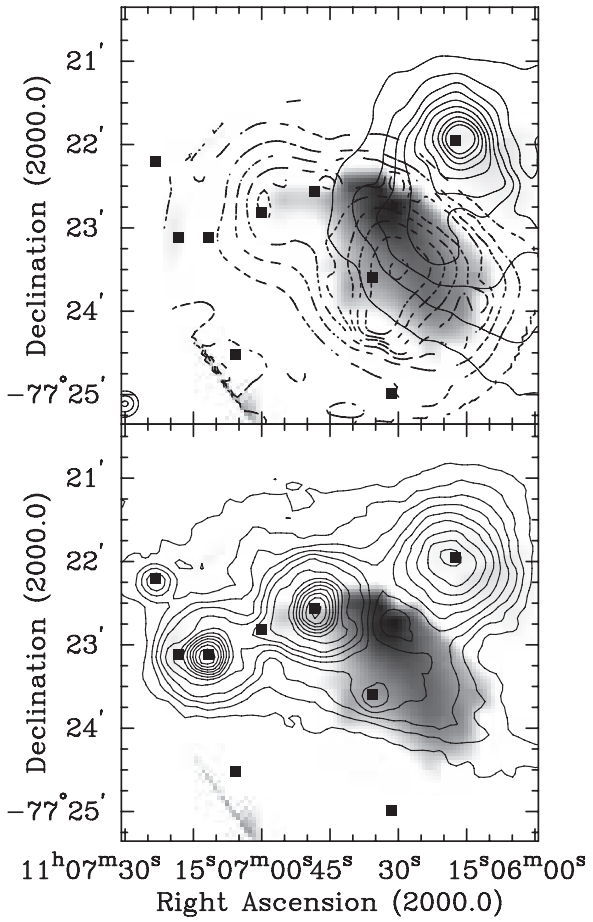

Figure 7. Top panel: optical emission from the European Southern Observatory Digitized Sky Survey (DSS2-red) image (solid contours) and the dense gas column density map (dashed contours) overlaid on an image of the excitation temperature determined from the N_2H^+ emission in gray scale. The excitation temperature gray scale runs from 5 (white) to 8.5 K (black). The DSS contours scale logarithmically, with each contour level a factor of 1.07 higher than the one below. The dense gas contours start at 8.5×10^{21} cm^{-2} and increment by 8.5×10^{21} cm^{-2}. Bottom panel: 70 μm continuum emission from *Spitzer* (contours) overlaid on an image of the excitation temperature determined from the N_2H^+ observations. Contour levels for the 70 μm emission scales logarithmically from 16 to 316 MJy sr^{-1}. Gray-scale levels for T_x are the same as in the top panel.

The morphology of the high T_x region matches much better with the strong gradient in the reflection nebulosity generated by IRS 2 to the northwest of the MMS-1 core (see Figure 7, top panel). The high T_x ridge runs along the northwest flank of the MMS-1 core, and it appears that this side of the core has been influenced by emission from IRS 2. Higher excitation temperatures can be caused by an increase in density (if the N_2H^+ is not fully thermalized) or by an increase in the kinetic temperature. With a luminosity of 3.4 $L_\odot$ (Lehtinen et al. 2001), IRS 2 is the most luminous source in the region, and at a distance of approximately 10^4 AU (in projection), it is close enough to the MMS-1 core to produce observable effects.

In the bottom panel of the Figure 7, T_x is plotted over the *Spitzer* 70 μm continuum emission (Belloche et al. 2006). The emission associated with IRS 6, IRS 4, and IRS 2 is clearly visible, as is the emission peak associated with MMS-1. The high T_x ridge is largely coincident with a region of extended weak (~30 MJy sr^{-1}) 70 μm emission, particularly toward the southwest. We can calculate an average dust temperature from the 70 μm flux density and the total column density. We use the typical dust opacity law

$$\kappa(\lambda) = \kappa_o \left(\frac{\lambda_o}{\lambda}\right)^\beta \tag{7}$$

with $\kappa_{160\,\mu m} = 0.23$ cm^{-2} g^{-1} and $\beta = 2$ (Terebey et al. 2009) and find $\kappa_{70\,\mu m} = 1.2$ cm^{-2} g^{-1}. Assuming single-temperature blackbody radiation, we find that dust with a temperature of 15.5 K can produce the observed 70 μm emission on the northwestern side of the MMS-1 core. On the southeastern side, where the 70 μm emission drops to 15 MJy sr^{-1}, dust with a temperature of 14.5 K is required. While the dust temperatures and the N_2H^+ excitation temperatures differ significantly (probably because the portion of the column responsible for the dust emission is not the deeply embedded dense gas), the morphology and particularly the gradients in the temperatures are similar, and we conclude that the high T_x ridge is a warmed (and not just density-enhanced) part of the MMS-1 core. IRS 2 appears to have enough luminosity to provide the observed warming. Assuming that all of the flux incident on the core material is absorbed, and that the warmed dust grains re-emit in the far-infrared with an emissivity described by Bianchi et al. (1999), dust grains with an initial temperature of 14 K can be warmed by approximately 2 K.

IRS 2 may also be responsible for the steep gradient in dense gas column density traced by N_2H^+, the 870 μm continuum emission of Belloche et al. (2011), and to a lesser degree, in the less dense gas traced by $C^{18}O$. The column density contours in maps derived from all three tracers are closely spaced and perpendicular to a line between IRS 2 and MMS-1, suggesting a sharp cutoff between the low column density environs of IRS 2 and the very high column density in the MMS-1 core. Radiation pressure from IRS 2 is two orders of magnitudes smaller than the dense core thermal pressure, so it is unlikely that this sharp boundary can be maintained by radiation alone. However, a wind from IRS 2 might provide the pressure confinement. The ram pressure of an isotropic wind from a mass-losing star can be described as

$$P_{\rm wind} = \frac{\dot{M}_{\rm wind}\, v_{\rm wind}}{4\pi D^2} = 11 \left(\frac{\dot{M}_{\rm wind}}{10^{-8}\, M_\odot\ {\rm yr}^{-1}}\right) \times \left(\frac{v_{\rm wind}}{500\ {\rm km\ s}^{-1}}\right) \left(\frac{D}{10^4\ {\rm AU}}\right) {\rm pPa}. \tag{8}$$

A mass loss rate of $10^{-8}\, M_\odot$ yr^{-1} is large but not unreasonable for G-type T Tauri stars. Mass accretion rates of 10^{-7}–$10^{-8}\, M_\odot$ yr^{-1} are common for these systems (Muzerolle et al. 2005; Hartmann et al. 2006) and the ratio between wind and accretion rates is typically 0.1.

So it is possible that a wind from IRS 2 could sweep up lower density gas and push it toward the MMS-1 dense core. Such a wind might also provide an external pressure to increase the density in the northwestern portion of the MMS-1 core, and in turn increase the excitation temperature of the N_2H^+ emission. The region of highest T_x, in the north part of the MMS-1 core, does not show strong 70 μm emission and may not be as warm as the rest of the ridge. This region is closest to the position of the kink on the blue lobe of the CO outflow, and closest to IRS 2, so it may be squeezed by pressures on both sides. Any interaction must be very gentle, though, as the N_2H^+ line widths in this region are among the narrowest in our map.

There is also a sharp gradient in dense gas column density on the opposite (i.e., southeastern) side of the MMS-1 dense

core. This gradient is also seen in the 870 μm continuum maps of Belloche et al. (2011). There is no obvious external source further to the southeast which might maintain this gradient.

Our virial analysis indicates that even in the absence of external pressure, the MMS-1 core is likely gravitationally unstable. The external pressure caused by the outflow from IRS 4 and potentially a wind from IRS 2 should further destabilize the core against collapse. Unless there exists a strong support mechanism which does not significantly enhance the dense gas velocity dispersion, this core must be actively collapsing, and the Class 0 source at its center must be accreting dense gas material.

5. CONCLUSIONS

1. We present observations of the Cederblad 110 star-forming region in the ($J = 1 \rightarrow 0$) line of N_2H^+. These observations indicate the presence of $13 \pm 3\,M_\odot$ of dense gas in the region. The typical excitation temperature of the emission is 7 K and based on the measured column density and spatial extent of the emission, the gas has an average density of 2×10^5 cm^{-3}.
2. We decompose the observed column density map into two structures (plus a background component); one structure has a mass of $9.3 \pm 0.6\,M_\odot$ and is nearly centered on the position of the Class 0 source MMS-1. The other structure has a mass of $1.6 \pm 0.3\,M_\odot$ and is nearly centered on the position of IRS 11. The dense core associated with MMS-1 cannot be supported against gravity by the kinetic energy inferred from the observed motions of the dense gas. The virial parameter $\alpha = 0.5$ for this core. The dense gas structure located near IRS 11 has $\alpha = 1.4$ and so may be stable against gravitational contraction.
3. We present ^{12}CO ($J = 1 \rightarrow 0$) observations of the outflow from IRS 4. The outflow is quite likely oriented nearly in the plane of the sky, but we detect some velocity-shifted emission, particularly blueward of line center. Combining our measurements with the ^{12}CO ($J = 3 \rightarrow 2$) data from Hiramatsu et al. (2007), we find the blue lobe of the outflow to have typical excitation temperatures of 8 K, typical column densities of 2×10^{19} cm^{-2}, and a total mass of $4.4 \times 10^{-3}\,M_\odot$.
4. The blue lobe of the outflow extends southwesterly from IRS 4 until it abruptly changes direction near the edge of the MMS-1 dense core. Though a dense core lacks the internal pressure to withstand a direct impact from an outflow, it is possible that the outflow's direction could be changed by a glancing interaction with the core. Farther to the southeast, at the head of the observed outflow, the dense gas line center velocities are blueshifted and the line widths are broadened, indicating a continuing interaction between the outflowing gas and the dense gas environs.
5. The reflection nebulosity produced against the MMS-1 dense core by IRS 2 and the enhanced 70 μm emission produced on the western side of the dense core indicate the IRS 2 is illuminating and heating the dense core. The strong gradient in dense gas column density from MMS-1 toward IRS 2 suggests that winds from IRS 2 may have swept lower density material toward the MMS-1 dense core and may be currently pressuring the MMS-1 dense core.
6. The high mass and small velocity dispersion of the MMS-1 dense core, coupled with the external pressures from outflows and winds, have likely made the MMS-1 core unstable to collapse. We conclude that this core is collapsing and depositing material onto its associated Class 0 source.

We are grateful to M. Hiramatsu for providing the ^{12}CO ($J = 3 \rightarrow 2$) data from Hiramatsu et al. (2007). E.F.L. acknowledges support from US National Science Foundation (NSF) Grant AST 03-0750, the Australia Telescope National Facility (ATNF) Distiguished Visitor Program, the Visiting Scientist Program at the Harvard-Smithsonian Center for Astrophysics, and the Bucknell University Office of the Dean of Arts & Sciences. K.L.T. acknowledges support from NSF Grant PHYS 05-52790, which supports the Bucknell University Research Experiences for Undergraduates (REU) program. T.L.B. acknowledges support from NSF Grant AST 07-08158. We thank the anonymous referee for comments that materially improved this work.

APPENDIX A

MEASURING THE OPTICAL DEPTH OF N_2H^+ ($J = 1 \rightarrow 0$) EMISSION

Due to hyperfine interactions between the nuclear spin of the nitrogen atoms and the rotation of the entire molecule, the $J = 1$ rotational energy level of N_2H^+ is split into seven distinct energy levels, and the $J = 0$ energy level is split into three. In principle, there are 15 allowed transitions between these two rotational states, but because the $J = 0$ levels are nearly degenerate in energy (splitting $<10^{-6}$ Hz; Daniel et al. 2006), only seven distinct components appear in the ($J = 1 \rightarrow 0$) spectrum.

One can calculate the statistical weights for each of these transitions, and assuming a common excitation temperature and low optical depth in each component, the ratios of the observed component intensities should match the ratios of statistical weights. In the case of very high optical depth (and a common excitation temperature), the ratios of the observed component intensities should be unity, as all components will be saturated. Between these extremes, the total optical depth and excitation temperature of the transition can be measured by comparing the observed line intensities with a simple model; as the total optical depth increases, the components with low statistical weight grow more quickly relative to the more saturated high-statistical-weight components.

A spectrum with such a fit produced with the "HFS" procedure in CLASS is shown in Figure 8. The fit corresponds well with most of the observed spectrum, though the two highest velocity (lowest frequency) components are not well reproduced. This "hyperfine anomaly" problem is well known and seen in N_2H^+ ($J = 1 \rightarrow 0$) spectra toward a large number of sources (e.g., Caselli et al. 1995). Daniel et al. (2006) show that these anomalies likely arise because of different Einstein coefficients for the excitation of the split energy levels, which particularly in the case of sub-thermal excitation, can lead to variations in the excitation temperature for each component.

Based on modeling by Daniel et al. (2007) and previous observations, the largest anomalies occur for the (F_1,F) = (1,2–1,2) and (1,0–1,1) transitions in that a common excitation temperature model overestimates the (F_1,F) = (1,2–1,2) intensity and underestimates the (F_1,F) = (1,0–1,1) intensity. In an effort to make the ratio between these two lines closer to unity (as is typically observed), the simple model is driven to higher total optical depth and lower common excitation temperature.

To prevent this known anomaly from biasing our optical depth and excitation temperature measurements, we chose to model

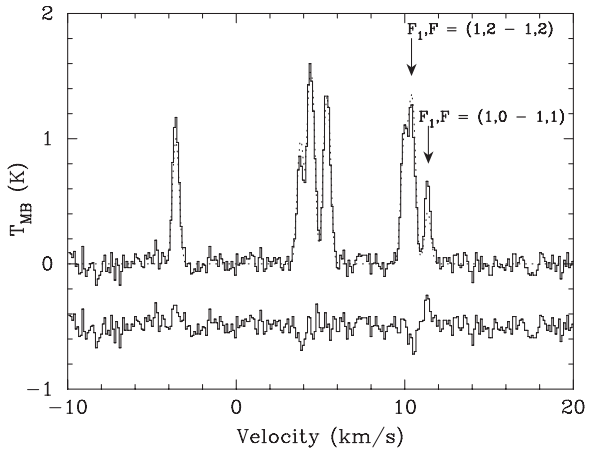

Figure 8. Typical N_2H^+ ($J = 1 \rightarrow 0$) spectrum in the Ced 110 region (solid line), overlaid with the best-fit seven-component "HFS" fit from the CLASS data analysis package (dashed line). The residual is displayed below the spectrum, displaced by 0.5 K for clarity. The $(F_1,F) = (1,2–1,2)$ and (1,0–1,1) components are not well fit with this model.

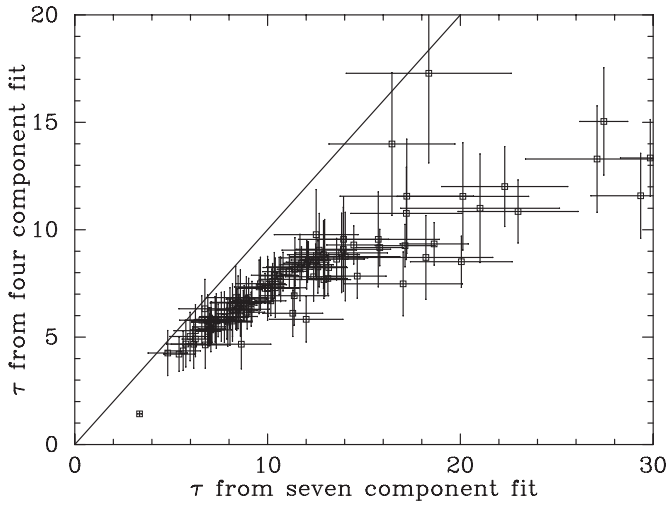

Figure 9. Comparison between the total ($J = 1 \rightarrow 0$) optical depth using the four-component fitting process described in the text and the standard seven-component fit. The seven-component fit consistently yields higher total optical depths than the four-component fit.

only the four lowest velocity (highest frequency) components of the ($J = 1 \rightarrow 0$) spectrum. We assume a constant excitation temperature for these four components as well as optical depth ratios according to their statistical weights. We calculate the total optical depth in these four transitions and then correct for the unmeasured optical depth in the high velocity (low frequency) triplet. In this way, we avoid the effects of trying to fit a single excitation temperature model to the most anomalous components.

A comparison between the two techniques shown in Figure 9 demonstrates that the optical depths measured using only four components are always lower than the optical depths derived from a seven-component fit. For moderate values ($\tau \sim 10$), the total optical depth from the four-component fit is typically ∼75% of the seven-component value.

APPENDIX B

WHAT IS THE SIZE OF A CORE?

The size of a dense core is an intrinsically interesting quantity, and it is an essential input for calculations of core mass, average density, and virial parameters. The *observed* size of a dense core is a function of the intrinsic core column density structure and the beam of the observing instrument. The smearing caused by the observing beam can have a substantial effect. A typical low-mass dense core has a size of ∼0.1 pc, so that its angular size at a distance of 200 pc is 100″, only a few times the beam size of single-dish telescopes and comparable to the resolution of star-counting extinction studies. At a distance of 2 kpc, a dense core has an angular size of 10″, comparable to the beam sizes of interferometric observations.

To determine a core's intrinsic size from observational data, one must assume an underlying structure for the core, then "deconvolve" to remove the smearing effects of the telescope beam, and finally "deproject" the column density distribution into a size estimate for the core. These operations often result in an inferred core size that is quite different from the observed core size. The purpose of this appendix is to investigate how well the inferred core size matches the true core size for a range of simple core models and observing beams.

By far the most common technique for determining core sizes involves deconvolving the observed core size by subtraction in quadrature with the observing beam, i.e.,

$$\Theta_{\rm core} = \sqrt{\Theta_{\rm obs}^2 - \Theta_{\rm beam}^2}, \quad \text{(B1)}$$

where $\Theta_{\rm core}$, $\Theta_{\rm obs}$, and $\Theta_{\rm beam}$ are the FWHM sizes of the intrinsic core column density distribution, the observed core column density distribution, and the telescope beam, respectively. The assumptions underlying this technique are that both the intrinsic core column density distribution and the telescope beam have Gaussian profiles. If the core column density distribution is in fact Gaussian, the core *volume* density distribution is also Gaussian, and $\Theta_{\rm core}$ is also the FWHM size of the volume density distribution. The primary advantages to this technique are that one can remove the smearing effects of the observing beam in a computationally simple way and that deprojection of the column density distribution into a volume density distribution is trivial.

Properly applied, this Gaussian assumption provides a reasonable approximation to physically plausible core geometries. Figure 10 shows the volume and column density distributions for four core geometries, all constrained to contain 1 $M_\odot$ within a radius $R_{\rm core} = 0.05$ pc. All density profiles are truncated at $r = R_{\rm core}$. The "constant" model has a constant density of 3.4×10^4 cm^{-3}. The "$1/r^2$" model is defined as $n(r) = n_{\rm core}(R_{\rm core}/r)^2$ with the density at the outer edge of the core, $n_{\rm core} = 1.1 \times 10^4$ cm^{-3}. The "Gaussian" model is defined as $n(r) = n_{\rm peak} e^{-\frac{r^2}{2\sigma^2}}$ with $n_{\rm peak} = 1.3 \times 10^5$ cm^{-3} and $\sigma = \frac{R_{\rm core}}{\sqrt{8\ln(2)}}$ (i.e., the FWHM size of the density distribution is equal to $R_{\rm core}$).The "critical BE" model is defined as a critically stable Bonnor– Ebert sphere with $T_{\rm BE} = 10$ K (Bonnor 1956). The peak volume density for this model is 2×10^5 cm^{-3}.

The volume density distributions determined from these four models agree within a factor of two for the outer parts of the core (i.e., $r > 0.6\ R_{\rm core}$), but diverge rather substantially toward the core center. However, since the central region is physically small and most of the core mass lies in the outer parts of the core, the column density distributions (as a function of impact parameter b) are more similar throughout nearly the whole core. The Gaussian model corresponds well with both the "critical BE" and "constant" models, differing from both by only 30% at the core center and by considerably less at larger impact

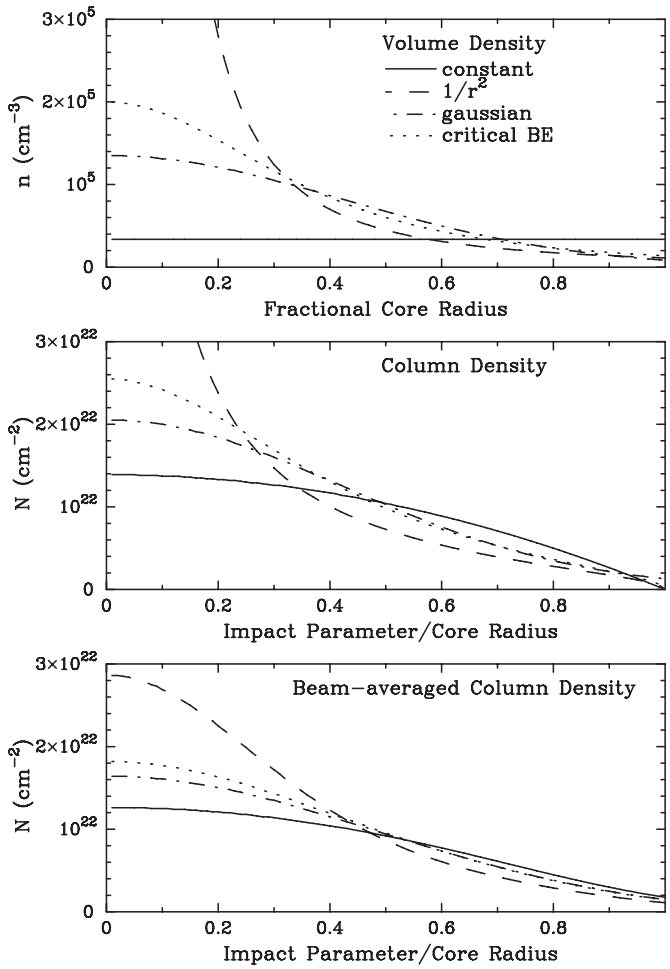

Figure 10. Top panel: number density vs. fractional core radius for four core models, each constrained to have $1\,M_\odot$ contained with $R_{\rm core} = 0.05$ pc. All density profiles are truncated at $r = R_{\rm core}$. See the text for the specific definitions for each model. Middle panel: column density vs. normalized impact parameter for the four models. Bottom panel: beam-averaged column density vs. normalized impact parameter. These profiles have been convolved with a Gaussian with FWHM $= \frac{R_{\rm core}}{2}$.

parameters. Even the "$1/r^2$" model differs by more than 50% only for the very inner core ($b < 0.2\ R_{\rm core}$).

When convolved with a moderate-sized observing beam, the differences between the four models become even smaller. The bottom panel of Figure 10 shows the "observed" column density profiles convolved with a Gaussian with FWHM $= R_{\rm core}/2$ ($34''$ for a distance of 150 pc). The column density profiles are nearly indistinguishable for $b > 0.4\ R_{\rm core}$, and even at the core center, the beam-averaged column densities of the 'Gaussian," "critical BE," and "constant" models differ by less than 20%. Observations of *very* high quality would be required in order to distinguish among these models.

Thus, the Gaussian model provides a reasonable approximation for core column density structures over a wide range of physical models. However, this correspondence is good *only* if the FWHM size of the Gaussian model is equal to $R_{\rm core}$. Choosing other values for the width of the Gaussian column density distribution will result in cores with profiles too flat or steep. The correspondence between these two quantities means that one can easily determine $R_{\rm core}$ by measuring the deconvolved FWHM size from core observations, as has been done by several authors (e.g., Benson & Myers 1989).

Many authors have instead estimated $R_{\rm core}$ from the deconvolved half-width at half-maximum (HWHM) size of the column density distribution (e.g., Caselli et al. 2002). This assignment leads to some rather puzzling inconsistences. First, it implies that the column density at the edge of the core is only one-half that at its peak (whereas for a model with $R_{\rm core}$ = FWHM, the column density at the core edge is 6% of peak). Second, a model with $R_{\rm core}$ = HWHM produces a very flat column density distribution—flatter than the constant column density model and *much* flatter than the "critical BE" model. Lastly, it is difficult to understand how to interpret the column density beyond the half-power contour. This material clearly has higher column density than the surrounding medium, but it has been excluded from the core by this restrictive definition. The differences can be quite substantial; integrating a Gaussian column distribution out to an impact parameter equal to the FWHM size encloses 86% of the total mass, while integrating out to the HWHM size encloses only 29%.

Therefore, we define the radius of the core, $R_{\rm core}$, as the deconvolved FWHM size of the observed column density distribution. We can use this quantity to estimate the mean density along the line of sight through the center of the core,

$$\overline{n} = \frac{N_{\rm max}}{2\ R_{\rm core}}, \tag{B2}$$

where $N_{\rm max}$ is the maximum measured column density.

If we assume further that the density distribution is Gaussian with the same width, we can calculate the virial mass self-consistently. The gravitational potential energy for this self-gravitating core is

$$U_{\rm grav} = -\frac{2}{3}\,\frac{G M_{\rm core}^2}{R_{\rm core}}, \tag{B3}$$

where $M_{\rm core}$ is the mass of the core within $r = R_{\rm core}$. Combining results with the kinetic energy determination presented in the text, and invoking the virial relation (assuming no other energy terms), we arrive at an expression for the virial mass of the core,

$$M_{\rm vir} = \frac{9}{2}\,\frac{\sigma_{\rm tot}^2\ R_{\rm core}}{G}, \tag{B4}$$

where the velocity dispersion $\sigma_{\rm tot}$ is defined above. We can express using observational units and quantities:

$$M_{\rm vir} = 188\ \Delta v_{\rm tot}^2\ R_{\rm core}, \tag{B5}$$

where $\Delta v_{\rm tot} = 8\ ln(2)\ \sigma_{\rm tot}$ is expressed in km s^{-1}, $R_{\rm core}$ in pc, and $M_{\rm vir}$ in $M_\odot$. The prefactor in this expression is about 10% smaller than the value derived assuming a constant density sphere.

REFERENCES

Allen, L., Megeath, S. T., Gutermuth, R., et al. 2007, in Protostars and Planets V, ed. B. Reipurth, D. Jewitt, & K. Keil (Tucson, AZ: Univ. Arizona Press), 361
Arce, H. G., & Sargent, A. I. 2006, ApJ, 646, 1070
Bacmann, A., Lefloch, B., Ceccarelli, C., et al. 2002, A&A, 389, L6
Bally, J., Walawender, J., Luhman, K. L., & Fazio, G. 2006, AJ, 132, 1923
Belloche, A., Parise, B., van der Tak, F. F. S., et al. 2006, A&A, 454, L51
Belloche, A., Schuller, F., Parise, B., et al. 2011, A&A, 527, A145
Benson, P. J., & Myers, P. C. 1989, ApJS, 71, 89
Bergin, E. A., Alves, J., Huard, T., & Lada, C. J. 2002, ApJ, 570, L101
Bianchi, S., Davies, J. I., & Alton, P. B. 1999, A&A, 344, L1

Bonnor, W. B. 1956, MNRAS, 116, 351
Bressert, E., Bastian, N., Gutermuth, R., et al. 2010, MNRAS, 409, L54
Carpenter, J. M. 2000, AJ, 120, 3139
Caselli, P., Benson, P. J., Myers, P. C., & Tafalla, M. 2002, ApJ, 572, 238
Caselli, P., Myers, P. C., & Thaddeus, P. 1995, ApJ, 455, L77
Caselli, P., Walmsley, C. M., Tafalla, M., Dore, L., & Myers, P. C. 1999, ApJ, 523, L165
Casertano, S., & Hut, P. 1985, ApJ, 298, 80
Cederblad, S. 1946, Meddelanden fran Lunds Astronomiska Observatorium Serie II, 119, 1
Chen, H., & Tokunaga, A. T. 1994, ApJS, 90, 149
Crapsi, A., Caselli, P., Walmsley, C. M., et al. 2005, ApJ, 619, 379
Daniel, F., Cernicharo, J., & Dubernet, M.-L. 2006, ApJ, 648, 461
Daniel, F., Cernicharo, J., Roueff, E., Gerin, M., & Dubernet, M. L. 2007, ApJ, 667, 980
Evans, N. J., II, Dunham, M. M., Jrgensen, J. K., et al. 2009, ApJS, 181, 321
Frerking, M. A., Langer, W. D., & Wilson, R. W. 1982, ApJ, 262, 590
Gutermuth, R. A., Megeath, S. T., Myers, P. C., et al. 2009, ApJS, 184, 18
Gutermuth, R. A., Megeath, S. T., Pipher, J. L., et al. 2005, ApJ, 632, 397
Haikala, L. K., Harju, J., Mattila, K., & Toriseva, M. 2005, A&A, 431, 149
Haisch, K. E., Barsony, M., Ressler, M. E., & Greene, T. P. 2006, AJ, 132, 2675
Hartmann, L., D'Alessio, P., Calvet, N., & Muzerolle, J. 2006, ApJ, 648, 484
Hiramatsu, M., Hayakawa, T., Tatematsu, K., et al. 2007, ApJ, 664, 964
Johnstone, D., Rosolowski, E., Tafalla, M., & Kirk, H. 2010, ApJ, 711, 655
Jorgensen, J. K., Johnstone, D., Kirk, H., et al. 2008, ApJ, 683, 822
Kainulainen, J., Lehtinen, K., & Harju, J. 2006, A&A, 447, 597
Kirk, H., & Myers, P. C. 2011, ApJ, 727, 64
Knude, J., & Hog, E. 1998, A&A, 338, 897
Kontinen, S., Harju, J., Heikkilä, A., & Haikala, L. K. 2000, A&A, 361, 704
Lada, C. J., & Lada, E. A. 2003, ARA&A, 41, 57
Ladd, N., Purcell, C., Wong, T., & Robertson, S. 2005, PASA, 22, 62
Lehtinen, K., Haikala, L. K., Mattila, K., & Lemke, D. 2001, A&A, 367, 311
Luhman, K. L. 2008, in Handbook of Star Forming Regions, ed. B. Reipurth (The Southern Sky ASP Monograph Publications, Vol. II) (San Francisco, CA: Astronomical Society of the Pacific), 169
Luhman, K. L., Allen, L. E., Allen, P. R., et al. 2008, ApJ, 675, 1375
Mattila, K., Liljestrom, T., & Toriseva, M. 1989, in Low-Mass Star Formation and Pre-Main-Sequence Objects, ed. B. Reipurth (Garching: ESO), 152
Mizuno, A., Hayakawa, T., Tachihara, K., et al. 1999, PASJ, 51, 859
Mizuno, A., Yamaguchi, R., Tachihara, K., et al. 2001, PASJ, 53, 1071
Muzerolle, J., Luhman, K. L., Briceño, C., Hartmann, L., & Calvet, N. 2005, ApJ, 625, 906
Persi, P., Marenzi, A. R., Gomez, M., & Olafsson, G. 2001, A&A, 376, 907
Persi, P., Marenzi, A. R., Olofsson, G., et al. 2000, A&A, 357, 219
Pontoppidan, K. M., & Dullemond, C. P. 2005, A&A, 435, 595
Prusti, T., Clark, F. O., Whittet, D. C. B., Laureijs, R. J., & Zhang, C. Y. 1991, MNRAS, 251, 303
Raga, A. C., de Gouveia Dal Pino, E. M., Noriega-Crespo, A., Mininni, P. D., & Velasquez, P. F. 2002, A&A, 392, 267
Reipurth, B., Nyman, L.-A., & Chini, R. 1996, A&A, 314, 258
Reipurth, B., Raga, A. C., & Heathcote, S. 1996, A&A, 311, 989
Robitaille, T. P., Whitney, B. A., Indebetouw, R., Wood, K., & Denzmore, P. 2006, ApJS, 167, 256
Sepulveda, I., Anglada, G., Estalella, R., et al. 2011, A&A, 527, A41
Schwartz, R. D., & Dopita, M. A. 1980, ApJ, 236, 543
Schwartz, R. D., Jones, B. F., & Sirk, M. 1984, AJ, 89, 1735
Tennekes, P. P., Harju, J., Juvela, M., & Toth, L. V. 2006, A&A, 456, 1037
Terebey, S., Fich, M., Noriega-Crespo, A., et al. 2009, ApJ, 696, 1918
Tsuribe, T., & Inutsaka, S. 1999, ApJ, 526, 307
Wang, S., Looney, L. W., Brandner, W., & Close, L. M. 2008, ApJ, 673, 315
Whittet, D. C. B., Prusti, T., Franco, G. A. P., et al. 1997, A&A, 327, 1194
Wolfram Research, Inc. 2008, Mathamatica, Version 7.0 (Champaign, IL: Wolfram Research)
Wu, Y., Wei, Y., Zhao, M., et al. 2004, A&A, 426, 503
Zinnecker, H., Krabbe, A., McCaughrean, M. J., et al. 1999, A&A, 352, L73